

Probing the Penetration Depth of Topological Surface States by Magnetic Impurity Scattering in V-doped Sb_2Te_3

Yidi Wang,^{1,*} Zeyu Ma,^{2,*} Pengcheng Chen,¹ Shiang Fang,¹ Yu Liu,¹ Yau Chuen Yam,¹
Christopher Eckberg,³ Joshua Samuel,³ Johnpierre Paglione,^{3,4} Mohammad Hamidian,¹ Cyrus
Hirjibehedin,^{1,5} Daniel T. Larson,¹ Efthimios Kaxiras,^{1,2} and Jennifer E. Hoffman^{1,2,†}

¹*Department of Physics, Harvard University, Cambridge, Massachusetts 02138, USA*

²*School of Engineering & Applied Sciences, Harvard University, Cambridge, Massachusetts 02138, USA*

³*Maryland Quantum Materials Center, Department of Physics, University of Maryland, College Park, Maryland 20742, USA*

⁴*Canadian Institute for Advanced Research, Toronto, Ontario M5G 1Z8, Canada*

⁵*London Centre for Nanotechnology, University College London (UCL), London WC1H 0AH, United Kingdom*
(Dated: March 17, 2026)

Topological insulators host Dirac surface states (SS) protected by time-reversal symmetry. Inter-surface hybridization can gap the SS and give rise to the quantum spin Hall effect in films that are sufficiently thin compared to the SS penetration depth. However, quantifying the SS penetration depth typically requires painstaking synthesis of multiple films with varying thickness. Here we introduce a direct method to probe the SS penetration depth in bulk crystals, by studying the interplay between SS and magnetic impurities in $(\text{V}_x\text{Sb}_{1-x})_2\text{Te}_3$. Using scanning tunneling microscopy and spectroscopy, we find that even sparse magnetic impurities ($\lesssim 0.25\%$ vanadium) can gap the Dirac SS. However, a single V impurity induces only localized states, and does not form an impurity band, so the gapped Dirac dispersion is preserved away from the impurity. In high magnetic fields, we observe an energy shift of the 0th Landau level and a suppression of quasiparticle lifetime at the Dirac point, indicating magnetic scattering of the SS. Crucially, by employing V impurities at different depths as precise scattering probes, we reveal the SS penetration depth on the sub-nanometer scale in a bulk crystal.

Three-dimensional topological insulators (TIs) host robust Dirac surface states (SS) whose spin-momentum locking offers potential for applications ranging from dissipationless spintronics [1, 2] to fault-tolerant quantum computation [3, 4]. Characterizing the SS penetration depth is essential for realizing and scaling these applications. Beyond theoretical predictions [5–9], most experimental approximations of the SS penetration depth have relied on time-consuming molecular-beam epitaxy (MBE) synthesis of multiple films with varying thickness, followed by transport [10–13], angle-resolved photoemission spectroscopy (ARPES) [14–20], terahertz spectroscopy [21, 22], or scanning tunneling microscopy/spectroscopy (STM/S) [23, 24] measurements of thickness-dependent effects (Table I). Direct imaging of SS scattering from magnetic impurities in different TI layers offers an alternative methodology to probe SS depth. However, the interpretation of single impurity effects was complicated by their large concentration in prior imaging studies of Cr- and V-doped $(\text{Bi,Sb})_2\text{Te}_3$ [25–27].

Here we introduce a direct probe of the SS penetration depth through scattering from dilute magnetic impurities in $(\text{V}_x\text{Sb}_{1-x})_2\text{Te}_3$. We perform STM/S measurements at $T = 4.6$ K to characterize the effects of isolated V impurities on topological SS. We find that V impurity states are spatially confined within ~ 2 nm, far smaller than the average V–V impurity separation, leaving clean regions where the SS are unobscured by an impurity band. At zero field, our dI/dV spectroscopy directly shows the

opening of a mass gap in the Dirac SS dispersion. In magnetic fields up to 8 T, our Landau level (LL) spectroscopy reveals an energy shift of the 0th LL across the entire measured area, consistent with the zero-field gap. We also observe a suppression of quasiparticle lifetime near the Dirac point (DP) energy E_D , which we attribute to exchange scattering from V impurities. Furthermore, by analyzing this scattering from V impurities in different atomic layers, we quantify the SS penetration depth in Sb_2Te_3 with sub-nanometer resolution, establishing a generalizable approach for determining SS depth in a broad range of topological materials.

Sb_2Te_3 has a quintuple-layer (QL) structure that cleaves at the van der Waals gap between two Te layers [Fig. 1(a)]. Single crystals were synthesized from ultrapure ($\geq 99.999\%$) elemental Sb and Te via a self-flux technique, with nominal V doping 1% [29]. The STM topography shows two primary defect types [Fig. 1(b)], which we identify as V dopants, distinguished from intrinsic Sb_{Te} defects by comparison with previous STM measurements on pristine samples [23, 27, 30]. At positive sample bias, the two types appear as triangular (Type I) and flower-like (Type II), whereas at negative sample bias, both types are less visible [Fig. 1(c, d)]. By counting the impurities on the surface, we find the V concentration of $(0.23 \pm 0.03)\%$ in each Sb layer (Fig. S1). Consistent with earlier studies [27, 31], we assign Type I (II) impurities to the V atoms in the first (second) Sb layer in the first QL. At our low concentration, the average lateral distance between V atoms in a full QL (i.e.

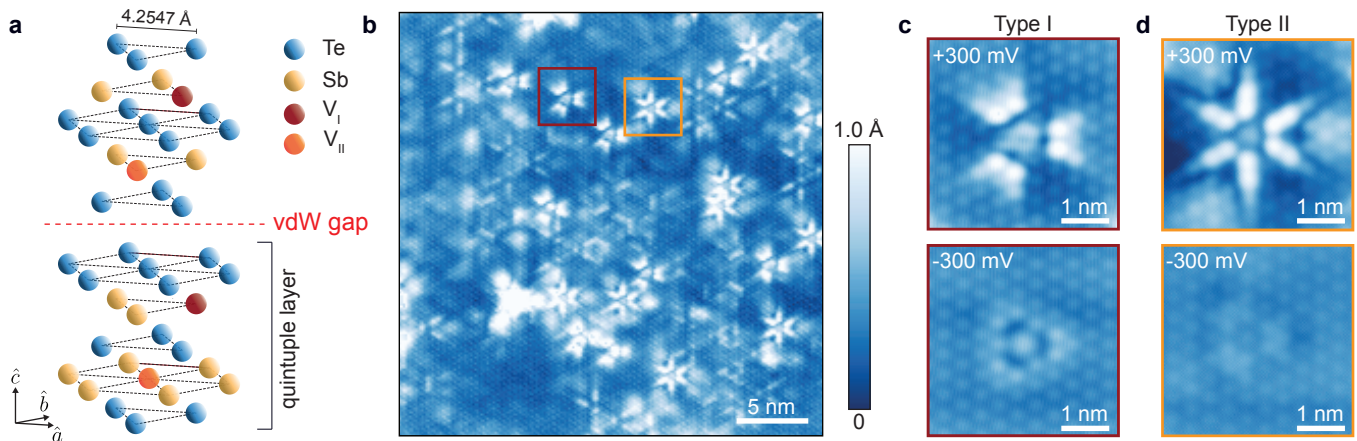


FIG. 1. Crystal structure and topography of $(V_xSb_{1-x})_2Te_3$ with $x \approx 0.23 \pm 0.03\%$. (a) Crystal structure of Sb_2Te_3 , with Type I and II vanadium impurities colored in red and orange, respectively. The lattice constants, determined by x-ray diffraction at 10 K, are $a = b = 4.2547(3)$ Å and $c = 30.268(3)$ Å, corresponding to 3 QLs [28]. (b) A 30×30 nm² STM topographic image of a cleaved Te-terminated surface, with typical Type I and II impurities boxed in red and orange, respectively. (c) Topographic images of a single Type I impurity at positive and negative sample biases. (d) Topographic images of a single Type II impurity at positive and negative sample biases. STM setpoints: $V_{\text{sample}} = 300$ mV, $I_{\text{set}} = 100$ pA in (b) and the top row of (c, d); $V_{\text{sample}} = -300$ mV, $I_{\text{set}} = 100$ pA in the bottom row of (c, d).

including both types) is 6 nm. Therefore, we can resolve intrinsic spectroscopy in clean areas without any V impurity.

To understand the impact of V impurities on the Dirac SS, we first investigate the local density of states (LDOS) in a clean region of $(V_xSb_{1-x})_2Te_3$. In general, differential conductance (dI/dV) is proportional to the LDOS as a function of energy. In Fig. 2(a), we show a representative dI/dV spectrum, at least 3 nm away from any V impurity. The sharp increase below +110 mV and above +350 mV indicates the onset of bulk valence and conduction bands, separated by a bulk energy gap $E_g \sim 240$ meV. Fig. 2(b) shows high-resolution dI/dV within the bulk gap, revealing a non-zero energy gap 2Δ with approximately linear energy dependence on either side of the gap. The gap is centered at $E_D \sim 176$ mV above the Fermi level, consistent with previous STS measurements of the DP [30, 31]. For comparison, we apply density functional theory (DFT) to calculate the band structure of pristine Sb_2Te_3 for a 10 QL slab, using VASP with Perdew-Burke Ernzerhof (PBE) pseudopotential [32–34] [Fig. 2(c)]. The agreement between DFT band structure and linearly dispersing dI/dV away from impurities indicates that the gapped Dirac SS dispersion is preserved away from the impurity.

We then measure dI/dV locally on both types of V impurity in Fig. 2(d). Type I impurity in the topmost Sb layer shows one pronounced dI/dV peak at ~ 240 mV, whereas Type II impurity in the second Sb layer shows peaks at both ~ 90 mV and ~ 240 mV. Together with a well-defined energy gap far from individual impurities, our measurements in the dilute-impurity regime supports that a single V impurity induces only localized states, in

contrast to $\sim 0.75\%$ V-doped Sb_2Te_3 , where the LDOS at the DP remains non-zero due to the formation of an in-gap impurity band [27].

Having established a zero-field mass gap, we use Landau level (LL) spectroscopy to further characterize the interaction between V impurities and Dirac SS. Perpendicular magnetic field B condenses the Dirac SS into discrete spectral peaks whose energies vary as the square root of B [23], and under sufficiently large B , the quantized LL energies become:

$$E_n - E_D = \begin{cases} \text{sgn}(n) \sqrt{2e\hbar v_D^2 |n| B + \Delta^2}, & n = \pm 1, \pm 2, \dots \\ \Delta, & n = 0 \end{cases}, \quad (1)$$

where n is the LL index, v_D is the velocity of SS electrons, and Δ is the mass term from magnetic-impurity-induced exchange scattering [26]. Fig. 3(a) displays dI/dV spectra in various B fields, measured far from any V impurity. We note that the 0th LL is shifted to a higher energy compared to the position expected for the ungapped SS, indicating a non-zero mass term.

We provide two independent arguments for the exchange scattering of Dirac SS from V impurities, based on the non-zero mass term Δ and the suppression of quasiparticle lifetime τ at the DP. First, we fit each LL spectrum, after background removal, as a sum of Lorentzian functions and plot the n^{th} LL energy vs. $\sqrt{|n|B}$ in Fig. 3(b). We then determine E_D from a linear fit to the $|n| \geq 2$ LLs, whose large spatial extension (> 20 nm) averages over local fluctuations of impurity density. Applying Eqn. 1, we extract Δ from the 0th LL, whose small spatial extension (~ 9 nm) reflects local doping variations. From this procedure, we obtain a

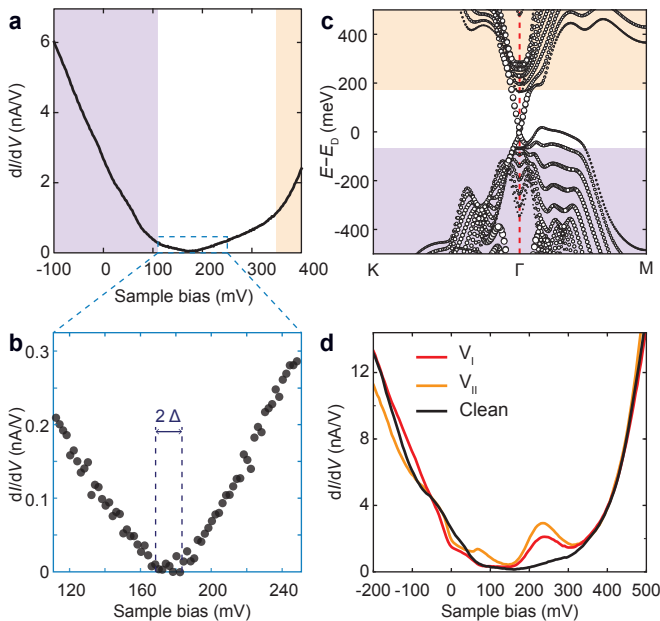


FIG. 2. Spectroscopic imaging of surface and impurity states. (a) A typical differential conductance dI/dV spectrum obtained 3 nm away from the nearest V impurity. The bulk band edges are identified from the local maxima of the second derivative, and are shaded in purple (valence band) and orange (conduction band). (b) Zoomed view of the energy window within the bulk gap (dashed box in (a)), showing a mass gap 2Δ at the DP and approximately linear dispersions on both sides. Dashed lines and arrow indicate the gap size and serve as guides to the eye. (c) DFT-calculated band structure of a pristine Sb_2Te_3 slab with 10 QLs. The marker size is proportional to the spectral weight projected onto the top QL atoms. The surface Dirac cone at Γ connects the bulk valence and conduction bands. Here, purple and orange shading denotes the same energy intervals below and above the DP where measured bulk bands onset in (a). The bands next to the Dirac cones between the shaded regions do not show up in the measured dI/dV due to their low surface spectral weight. (d) Average dI/dV spectra over a clean area (black), Type I impurity (red), and Type II impurity (orange). Setpoints: $V_{\text{sample}} = -100$ mV, $I_{\text{set}} = 500$ pA. Lock-in zero-to-peak amplitude $V_{\text{exc}} = 2$ mV in (a,b) and $V_{\text{exc}} = 5$ mV in (d).

position-dependent mass term Δ ranging from approximately 9 to 13 meV, with an estimated uncertainty of ~ 1.5 meV arising from errors in the LL peak fitting and the linear fitting. The mass term consists of two parts: $\Delta = \frac{1}{2}JM_z/\mu_B + \frac{1}{2}g_s\mu_B B$, where J is the strength of exchange interaction between magnetic impurities and SS electrons, M_z is the local magnetization in the z direction, and g_s is the Landé factor of SS electrons. Under our applied magnetic fields, the Zeeman term $\frac{1}{2}g_s\mu_B|B|$ is relatively small (< 1 mV) [26], and therefore Δ arises primarily from the exchange interaction between polarized V impurities and SS electrons. Since the size of the mass term should increase with impurity density [25, 35], our result is consistent with the 16 meV mass term ob-

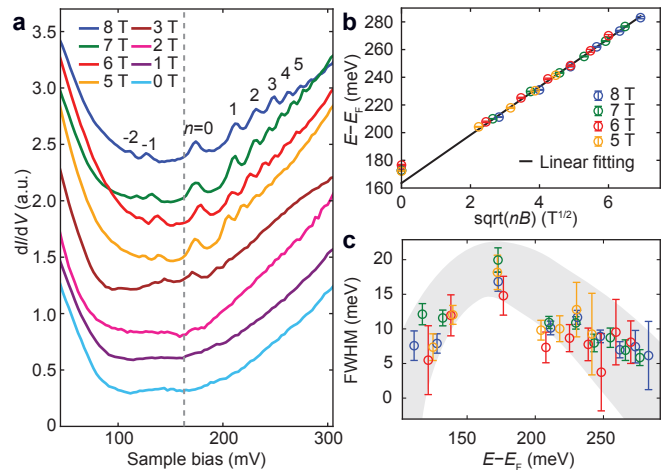


FIG. 3. Evidence of exchange scattering of Dirac SS. (a) dI/dV measurement of Landau quantization in magnetic field B up to 8 T, applied perpendicular to the surface. Spectra at each field are measured at different sample locations but all at least 3 nm away from the nearest V impurity. The curves are shifted vertically for clarity. The gray dashed line indicates the DP energy E_D , which would be the field-independent 0th LL energy without mass acquisition. A clear shift of the 0th LL towards higher energy signals a mass gap opening in the Dirac SS. (b) Extracted LL energies plotted as a function of \sqrt{nB} for spectra from 5–8 T. The dashed line shows a linear fit to the $|n| \geq 2$ LLs at high magnetic fields, which we use to determine E_D . The energy offset of the zeroth LL relative to this linear trend yields the mass term Δ . (c) FWHM of the LL peaks extracted from the 5–8 T data in (a). We obtain the LL peak positions and widths by fitting the spectra, after background removal, with a sum of Lorentzian functions. The gray dashed line indicates E_D , same as in (a). Setpoint: $V_{\text{sample}} = -100$ mV, $I_{\text{set}} = 2$ nA, lock-in zero-to-peak amplitude $V_{\text{exc}} = 3$ mV, which is smaller than the fitted peak width.

served in $(\text{V}_x\text{Sb}_{1-x})_2\text{Te}_3$ with $x \sim 0.75\%$ [27].

Next, we examine quasiparticle lifetime τ of the Dirac SS. In pristine Sb_2Te_3 , topological protection of the SS restricts the available relaxation channels imposed by conservation laws. As a result, intraband electron–electron interaction dominates and produces an enhanced lifetime near E_D [23, 36]. In contrast, by fitting the full width at half maximum (FWHM) of LL peaks as a function of energy in Fig. 3(c), we find that the peak width is maximal at the 0th LL and decreases for $|n| > 0$, indicating a suppression of τ near E_D in $(\text{V}_x\text{Sb}_{1-x})_2\text{Te}_3$. In principle, τ can be influenced by electron–phonon coupling, electron–electron interactions, intrinsic disorder, etc. We rule out these time-reversal-preserving mechanisms and attribute the reduced τ to the exchange interaction that breaks time-reversal symmetry. First, electron–phonon coupling does not play a role here, because it modifies τ only above a cutoff phonon energy that lies well outside our energy window of interest [23]. Second, upon finite-range mass acquisi-

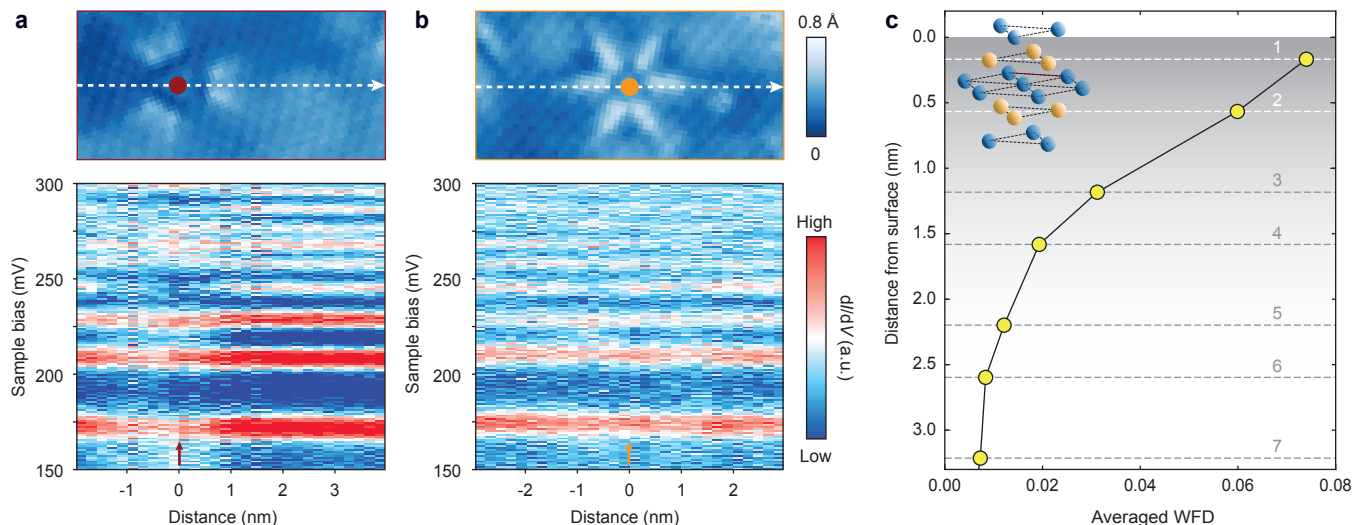


FIG. 4. Probing SS depth from LL suppression around V impurities. (a, b) LL spectra at 8 T acquired along line cuts passing through Type I (a) and Type II (b) impurities, with the background subtracted. The red and orange arrows mark the impurity centers. Top panels show the corresponding topographic images, where the white dashed arrows denote the direction of the line cuts and the colored dots indicate the impurity centers. (c) DFT-calculated real-space distribution of the averaged surface-state wave-function density (WFD) on the top 7 Sb layers (top 4 QLs). Horizontal dashed lines indicate the Sb layer index measured from the surface. The color gradient in the background indicates the decay of SS. Setpoint in (a, b): $V_{\text{sample}} = -100$ mV, $I_{\text{set}} = 400$ pA, lock-in zero-to-peak amplitude $V_{\text{exc}} = 3$ mV. STM setpoint for the topographic insets in (a, b): $V_{\text{sample}} = 200$ mV, $I_{\text{set}} = 50$ pA, $B = 8$ T.

tion in $(V_x\text{Sb}_{1-x})_2\text{Te}_3$, intraband electron-electron interaction is considerably weakened, as the opening of a mass gap further reduces the available low-energy relaxation channels by modifying the Dirac spectrum. Finally, interband electron-electron interaction and intrinsic disorder from substitutional defects are incompatible with our data, as both mechanisms produce a monotonic decrease in τ away from the Fermi energy E_F [23, 36, 37]. On the other hand, a magnetic impurity can mix the opposite helicities from two Dirac branches at E_D [38–40], where SS are maximally susceptible to spin-dependent perturbations, and exchange-mediated spin fluctuations lead to lifetime suppression [41, 42]. Therefore, our observation of reduced τ reflects an enhanced magnetic scattering near E_D with a non-zero exchange coupling strength J .

To explicitly characterize how V impurities perturb the SS, we measure the LL intensity using dI/dV linecuts across both Type I and Type II impurities at 8 T. For Type I impurities, we observe a clear and highly localized suppression of LLs within a radius of 2 nm, as shown in Fig. 4(a). This behavior is qualitatively different from the previously reported LL suppression caused by non-magnetic Ag adatoms, where individual Ag atom exerts little effect on the LLs, and a global suppression of the SS emerges only when the average impurity distance is comparable to the magnetic length [43].

More importantly, the z -dependence of this LL suppression provides a direct probe of the SS penetration depth. As shown in Fig. 4(b), LLs remain essentially

intact when the tip crosses a Type II impurity. The difference of LL suppression between Type I and Type II impurities in the 1st and 2nd Sb layer within one QL (≈ 1.0 nm) reveals the sharpness of the exponential decay of the SS [44], and demonstrates that the SS wavefunction is concentrated predominantly within the top sub-nanometer of the crystal.

To examine how SS wavefunction decays into the bulk, we apply DFT calculations and compare with the probed SS depth. We obtain the layer-resolved wavefunction density by integrating the spectral weight of the Dirac bands near Γ point, within roughly ± 120 meV around E_D . Fig. 4(c) shows that the SS weight drops rapidly within the 1st QL. Compared to that in the top Sb layer, SS wavefunction density decreases approximately 22% and 67% in the 2nd and the 3rd Sb layers. The fast decay indicates that the SS are concentrated in the top layers of the 1st QL, and hence produces a stronger exchange scattering with Type I impurities. In addition, we find that the top four Sb layers contribute 75% of the SS wavefunction density, consistent with previous estimation [23, 24] and derivation [45] of the SS depth (Table II for details).

Quantifying SS penetration depth from V-induced exchange scattering provides new insights on the debate of the impurity magnetism effect in three-dimensional TIs [27, 46, 47]. As we have demonstrated in the field-free case, impurity states are spatially localized and energetically isolated from E_D [Fig. 2(d)]. Under high magnetic

fields, the impurity states remain localized, while the exchange interaction between the magnetic moments of V impurities and SS quasiparticles produces a finite mass term and suppresses τ near E_D through spatially averaged exchange scattering. In addition, we do not observe the suppression of τ at the impurity-state energy [Fig. 3(c)], which further supports little hybridization between impurity states and the SS. Therefore, our observation that two types of V impurities at different depths provide different SS suppression suggests that the suppression mainly comes from the magnetic exchange scattering.

In summary, our spectroscopic imaging shows a confined spatial distribution of local electronic impurity states, beyond which the SS recover a well-defined, gapped Dirac dispersion. Under high out-of-plane magnetic fields, LL spectroscopy verifies a non-zero mass term and demonstrates the suppression of quasiparticle lifetime at the 0th LL energy, both of which results from the exchange scattering from V impurities. Furthermore, direct spectroscopic imaging across impurities at different depths yields a sharp difference of the scattering-induced LL suppression. The contrast in the local LL suppression indicates that the SS are strongly localized within 2 nm from the surface, corroborated by DFT calculations of SS wavefunction density decay. Our method of studying exchange scattering effect from isolated magnetic impurities serves as a universal tool for characterizing topological SS, and may aid in the exploration of new topological candidates for vast potential spintronics and magnetoelectronics applications.

ACKNOWLEDGMENTS

STM experiments at Harvard were supported by the U.S. National Science Foundation under Grant No. DMR-110623. DTL and EK acknowledge support from the US Army Research Office (ARO) MURI project under Grant No. W911NF-21-0147. Crystal synthesis at the University of Maryland was supported by the Gordon and Betty Moore Foundation's EPiQS Initiative Grant No. GBMF9071, the Air Force Office of Scientific Research Grant No. FA9950-22-1-0023 and the Maryland Quantum Materials Center.

* These authors contributed equally to this work.

† Corresponding author: jhoffman@physics.harvard.edu

- [1] L. Šmejkal, Y. Mokrousov, B. Yan, and A. H. MacDonald, Topological antiferromagnetic spintronics, *Nature Physics* **14**, 242 (2018).
 [2] Q. He, T. L. Hughes, N. P. Armitage, Y. Tokura, and K. L. Wang, Topological spintronics and magnetoelectronics, *Nature Materials* **21**, 15 (2022).

- [3] J. Alicea, Y. Oreg, G. Refael, F. von Oppen, and M. P. A. Fisher, Non-Abelian statistics and topological quantum information processing in 1D wire networks, *Nature Physics* **7**, 412 (2011).
 [4] C. Nayak, S. H. Simon, A. Stern, M. Freedman, and S. Das Sarma, Non-abelian anyons and topological quantum computation, *Reviews of Modern Physics* **80**, 1083 (2008).
 [5] S. Urazhdin, D. Bilc, S. Mahanti, S. Tessmer, T. Kyratsi, and M. Kanatzidis, Surface effects in layered semiconductors Bi₂Se₃ and Bi₂Te₃, *Physical Review B* **69**, 085313 (2004).
 [6] H. Zhang, C.-X. Liu, X.-L. Qi, X. Dai, Z. Fang, and S.-S. Zhang, Topological insulators in Bi₂Te₃, Bi₂Se₃ and Sb₂Te₃ with a single Dirac cone on the surface, *Nature Physics* **5**, 438 (2009).
 [7] W. Zhang, R. Yu, H.-J. Zhang, X. Dai, and Z. Fang, First-principles studies of the three-dimensional strong topological insulators Bi₂Te₃, Bi₂Se₃ and Sb₂Te₃, *New Journal of Physics* **12**, 065013 (2010).
 [8] M. M. Otrokov, I. P. Rusinov, M. Blanco-Rey, M. Hoffmann, A. Y. Vyazovskaya, S. V. Eremeev, A. Ernst, P. M. Echenique, A. Arnau, and E. V. Chulkov, Unique thickness-dependent properties of the van der Waals interlayer antiferromagnet MnBi₂Te₄ films, *Physical Review Letters* **122**, 107202 (2019).
 [9] H.-P. Sun, C. M. Wang, S.-B. Zhang, R. Chen, Y. Zhao, C. Liu, Q. Liu, C. Chen, H.-Z. Lu, and X. C. Xie, Analytical solution for the surface states of the antiferromagnetic topological insulator MnBi₂Te₄, *Physical Review B* **102**, 241406 (2020).
 [10] Y. Takagaki, A. Giussani, K. Perumai, R. Calarco, and K.-J. Friedland, Robust topological surface states in Sb₂Te₃ layers as seen from the weak antilocalization effect, *Physical Review B* **86**, 125137 (2012).
 [11] B. A. Assaf, F. Katmis, P. Wei, B. Satpati, Z. Zhang, S. P. Bennett, V. Harris, J. S. Mooera, and D. Heman, Quantum coherent transport in SnTe topological crystalline insulator thin films, *Applied Physics Letters* **105**, 102108 (2014).
 [12] T. Liu, Y. Li, L. Gu, J. Dng, H. Chang, P. A. P. Janantha, B. Kalinikos, V. Novosad, A. Hoffmann, R. Wu, C. L. Chien, and M. Wu, Nontrivial nature and penetration depth of topological surface states in SmB₆ thin films, *Physical Review Letters* **120**, 207206 (2018).
 [13] F. van Veen, S. Kölling, S. R. de Wit, R. Metsch, D. Rosenbach, C. Li, and A. Brinkman, Observation of the surface hybridization gap in the electrical transport properties of the ultrathin topological insulator (Bi_{1-x}Sb_x)₂Te₃, *Physical Review B* **112**, 045425 (2025).
 [14] Y.-Y. Li, G. Wang, X.-G. Zhu, M.-H. Liu, C. Ye, X. Chen, Y.-Y. Wang, K. He, L.-L. Wang, X.-C. Ma, H.-J. Zhang, X. Dai, Z. Fang, X.-C. Xie, Y. Liu, X.-L. Qi, J.-F. Jia, S.-S. Zhang, and Q.-K. Xue, Intrinsic topological insulator Bi₂Te₃ thin films on Si and their thickness limit, *Advanced Materials* **22**, 4002 (2010).
 [15] Y. Zhang, K. He, C.-Z. Chang, C.-L. Song, L.-L. Wang, X. Chen, J.-F. Jia, Z. Fang, X. Dai, W.-Y. Shan, S.-Q. Shen, Q. Niu, X.-L. Qi, S.-C. Zhang, X.-C. Ma, and Q.-K. Xue, Crossover of the three-dimensional topological insulator Bi₂Se₃ to the two-dimensional limit, *Nature Physics* **6**, 584 (2010).
 [16] P. Dziawa, B. J. Kowalski, K. Dybko, R. Buczko, A. Szczerbakow, M. Szot, E. Lusakowska, T. Balasub-

- ramanian, B. M. Wojek, M. H. Berntsen, O. Tjernberg, and T. Story, Topological crystalline insulator states in $\text{Pb}_{1-x}\text{Sn}_x\text{Se}$, *Nature Materials* **11**, 1023 (2012).
- [17] Y. Gong, K. Zhu, Z. Li, Y. Zang, X. Feng, D. Zhang, C. Song, L. Wang, W. Li, X. Chen, X.-C. Ma, Q.-K. Xue, Y. Xu, and K. He, Experimental evidence of the thickness- and electric-field-dependent topological phase transitions in topological crystalline insulator $\text{SnTe}(111)$ thin films, *Nano Research* **11**, 6045 (2018).
- [18] S. Ciocys, T. Morimoto, R. Mori, K. Gotlieb, Z. Hussain, J. G. Analytis, J. E. Moore, and A. Lanzara, Manipulating long-lived topological surface photovoltage in bulk-insulating topological insulators Bi_2Se_3 and Bi_2Te_3 , *npj Quantum Materials* **5**, 16 (2020).
- [19] Z. Wang, T. Zhou, T. Jiang, H. Sun, Y. Zang, Y. Gong, J. Zhang, M. Tong, X. Xie, Q. Liu, C. Chen, K. He, and Q.-K. Xue, Dimensional crossover and topological nature of the thin films of a three-dimensional topological insulator by band gap engineering, *Nano Letters* **19**, 4627 (2019).
- [20] R. Xu, Y. Bai, J. Zhou, X. Gu, N. Qin, Z. Yin, X. Du, Q. Zhang, W. Zhao, Y. Li, Y. Wu, C. Ding, L. Wang, Z. Liang Aiji and Liu, Y. Xu, X. Feng, K. He, y. Chen, and Y. Lixian, Evolution of the electronic structure of ultrathin MnBi_2Te_4 films, *Nano Letters* **22**, 6320 (2022).
- [21] L. Wu, M. Brahlek, R. Valdés Aguilar, A. V. Stier, C. M. Morris, L. Y., L. S. Bilbro, N. Bansal, S. Oh, and N. P. Armitage, A sudden collapse in the transport lifetime across the topological phase transition in $(\text{Bi}_{1-x}\text{In}_x)_2\text{Se}_3$, *Nature Physics* **9**, 410 (2013).
- [22] H. Park, S. Rho, J. Kim, H. Kim, D. Kim, C. Kang, and M.-H. Cho, Topological surface-dominated spintronic THz emission in topologically nontrivial $\text{Bi}_{1-x}\text{Sb}_x$ films, *Advanced Science* **9**, 2200948 (2022).
- [23] Y. Jiang, Y. Wang, M. Chen, Z. Li, C. Song, K. He, L. Wang, X. Chen, X. Ma, and Q.-K. Xue, Landau quantization and the thickness limit of topological insulator thin films of Sb_2Te_3 , *Physical Review Letters* **108**, 016401 (2012).
- [24] T. Zhang, J. Ha, N. Levy, Y. Kuk, and J. Stroscio, Electric-field tuning of the surface band structure of topological insulator Sb_2Te_3 thin films, *Physical Review Letters* **111**, 056803 (2013).
- [25] I. Lee, C. K. Kim, J. Lee, S. J. L. Billinge, R. Zhong, J. A. Schneeloch, T. Liu, T. Valla, J. M. Tranquada, G. Gu, and J. C. S. Davis, Imaging Dirac-mass disorder from magnetic dopant atoms in the ferromagnetic topological insulator $\text{Cr}_x(\text{Bi}_{0.1}\text{Sb}_{0.9})_{2-x}\text{Te}_3$, *PNAS* **112**, 1316 (2015).
- [26] Y. Jiang, C. Song, Z. Li, M. Chen, R. L. Greene, K. He, L. Wang, X. Chen, X. Ma, and Q.-K. Xue, Mass acquisition of Dirac fermions in magnetically doped topological insulator Sb_2Te_3 films, *Physical Review B* **92**, 195418 (2015).
- [27] P. Sessi, R. R. Biswas, T. Bathon, O. Storz, S. Wilfert, A. Barla, K. A. Kokh, O. E. Tereshchenko, K. Fauth, M. Bode, and A. V. Balatsky, Dual nature of magnetic dopants and competing trends in topological insulators, *Nature Communications* **7**, 12027 (2016).
- [28] A. N. Mansour, W. Wong-Ng, Q. Huang, W. Tang, A. Thompson, and J. Sharp, Structural characterization of Bi_2Te_3 and Sb_2Te_3 as a function of temperature using neutron powder diffraction and extended X-ray absorption fine structure techniques, *Journal of Applied Physics* **116**, 083513 (2014).
- [29] N. P. Butch, K. Kirshenbaum, P. Syers, A. B. Sushkov, G. S. Jenkins, H. D. Drew, and J. Paglione, Strong surface scattering in ultrahigh-mobility Bi_2Se_3 topological insulator crystals, *Physical Review B* **81**, 241301 (2010).
- [30] Y. Jiang, Y. Y. Sun, M. Chen, Y. Wang, Z. Li, C. Song, K. He, L. Wang, X. Chen, Q.-K. Xue, X. Ma, and S. B. Zhang, Fermi-level tuning of epitaxial Sb_2Te_3 thin films on graphene by regulating intrinsic defects and substrate transfer doping, *Physical Review Letters* **108**, 066809 (2012).
- [31] W. Zhang, D. West, S. H. Lee, Y. Qiu, C.-Z. Chang, J. S. Moodera, Y. S. Hor, S. Zhang, and W. Wu, Electronic fingerprints of Cr and V dopants in the topological insulator Sb_2Te_3 , *Physical Review B* **98**, 115165 (2018).
- [32] G. Kresse and J. Furthmüller, Efficient iterative schemes for ab initio total-energy calculations using a plane-wave basis set, *Physical Review B* **54**, 11169 (1996).
- [33] G. Kresse and D. Joubert, From ultrasoft pseudopotentials to the projector augmented-wave method, *Physical Review B* **59**, 1758 (1999).
- [34] J. P. Perdew, K. Burke, and M. Ernzerhof, Generalized gradient approximation made simple, *Physical Review Letters* **77**, 3865 (1996).
- [35] D. A. Abanin and D. A. Pesin, Ordering of magnetic impurities and tunable electronic properties of topological insulators, *Physical Review Letters* **106**, 136802 (2011).
- [36] C. Pauly, C. Saunus, M. Liebmann, and M. Morgenstern, Spatially resolved Landau level spectroscopy of the topological Dirac cone of bulk-type $\text{Sb}_2\text{Te}_3(0001)$: Potential fluctuations and quasiparticle lifetime, *Physical Review B* **92**, 085140 (2015).
- [37] T. Hanaguri, K. Igarashi, M. Kawamura, H. Takagi, and T. Sasagawa, Momentum-resolved Landau-level spectroscopy of Dirac surface state in Bi_2Se_3 , *Physical Review B* **82**, 081305 (2010).
- [38] Q. Liu, C.-X. Liu, C. Xu, X.-L. Qi, and S.-C. Zhang, Magnetic impurities on the surface of a topological insulator, *Physical Review Letters* **102**, 156603 (2009).
- [39] X. Zhou, C. Fang, W.-F. Tsai, and J. Hu, Theory of quasiparticle scattering in a two-dimensional system of helical Dirac fermions: Surface band structure of a three-dimensional topological insulator, *Physical Review B* **80**, 245317 (2009).
- [40] P. Thalmeier and A. Akbari, Gapped Dirac cones and spin texture in thin film topological insulator, *Physical Review Research* **2**, 033002 (2020).
- [41] Y.-H. Li and R. Cheng, Spin fluctuations in quantized transport of magnetic topological insulators, *Physical Review Letters* **126**, 026601 (2021).
- [42] S. Kudła, A. Dyrdał, V. K. Dugaev, J. Berakdar, and J. Barnaś, Conduction of surface electrons in a topological insulator with spatially random magnetization, *Physical Review B* **100**, 205428 (2019).
- [43] P. Cheng, C. Song, T. Zhang, Y. Zhang, Y. Wang, J.-F. Jia, J. Wang, Y. Wang, B.-F. Zhu, X. Chen, X. Ma, K. He, L. Wang, X. Dai, Z. Fang, X. Xie, X.-L. Qi, C.-X. Liu, S.-C. Zhang, and Q.-K. Xue, Landau quantization of topological surface states in Bi_2Se_3 , *Physical Review Letters* **105**, 076801 (2010).
- [44] C.-X. Liu, X.-L. Qi, H. Zhang, X. Dai, Z. Fang, and S.-C. Zhang, Model Hamiltonian for topological insulators, *Physical Review B* **82**, 045122 (2010).

- [45] J. Linder, T. Yokoyama, and A. Sudbø, Anomalous finite size effects on surface states in the topological insulator Bi_2Se_3 , *Physical Review B* **80**, 205401 (2009).
- [46] T. Valla, Z.-H. Pan, D. Gardner, Y. S. Lee, and S. Chu, Photoemission spectroscopy of magnetic and nonmagnetic impurities on the surface of the Bi_2Se_3 topological insulator, *Physical Review Letters* **108**, 117601 (2012).
- [47] L. A. Wray, S.-Y. Xu, Y. Xia, D. Hsieh, A. V. Fedorov, Y. S. Hor, R. J. Cava, A. Bansil, H. Lin, and M. Z. Hasan, A topological insulator surface under strong Coulomb, magnetic and disorder perturbations, *Nature Physics* **7**, 32 (2011).
- [48] P. E. Blöchl, Projector augmented-wave method, *Physical Review B* **50**, 17953 (1994).
- [49] V. Wang, N. Xu, J.-C. Liu, G. Tang, and W.-T. Geng, VASPKIT: A user-friendly interface facilitating high-throughput computing and analysis using VASP code, *Computer Physics Communications* **267**, 108033 (2021).
- [50] G. Yao, Z. Luo, F. Pan, W. Xu, Y. P. Feng, and X.-s. Wang, Evolution of topological surface states in antimony ultra-thin films, *Scientific Reports* **3**, 2010 (2013).
- [51] H. Yi, Y.-F. Zhao, Y.-T. Chan, J. Cai, R. Mei, X. Wu, Z.-J. Yan, L.-J. Zhou, R. Zhang, Z. Wang, S. Paolini, R. Xiao, K. Wang, A. R. Richardella, J. Singleton, L. E. Winter, T. Prokscha, Z. Salman, A. Suter, P. P. Balakrishnan, A. J. Grutter, M. H. W. Chan, N. Samarth, X. Xu, W. Wu, C.-X. Liu, and C.-Z. Chang, Interface-induced superconductivity in magnetic topological insulators, *Science* **383**, 634 (2024).
- [52] N. Shumiya, M. S. Hossain, J.-X. Yin, Z. Wang, M. Litskevich, C. Yoon, Y. Li, Y. Yang, Y.-X. Jiang, G. Cheng, Y.-C. Lin, Q. Zhang, Z.-J. Cheng, T. A. Cochran, D. Multer, X. P. Yang, B. Casas, T.-R. Chang, T. Neupert, Z. Yuan, S. Jia, H. Lin, N. Yao, L. Balicas, F. Zhang, Y. Yao, and M. Z. Hasan, Evidence of a room-temperature quantum spin Hall edge state in a higher-order topological insulator, *Nature Materials* **21**, 1111 (2022).
- [53] S. Lee, V. Stanev, X. Zhang, D. Stasak, J. Flowers, J. S. Higgins, S. Dai, T. Blum, X. Pan, V. M. Yakovenko, J. Paglione, R. L. Greene, V. Galitski, and I. Takeuchi, Perfect Andreev reflection due to the Klein paradox in a topological superconducting state, *Nature* **570**, 344 (2019).
- [54] G. Bendt, S. Zastrow, K. Nielsch, P. S. Mandal, J. Sánchez-Barriga, O. Rader, and S. Schulz, Deposition of topological insulator Sb_2Te_3 films by an MOCVD process, *Journal of Materials Chemistry A* **2**, 8215 (2014).
- [55] G. Wang, X. Zhu, J. Wen, X. Chen, K. He, L. Wang, X. Ma, Y. Liu, X. Dai, Z. Fang, J. Jia, and Q. Xue, Atomically smooth ultrathin films of topological insulator Sb_2Te_3 , *Nano Research* **3**, 874 (2010).
- [56] C. Pauly, G. Bihlmayer, M. Liebmann, M. Grob, A. Georgi, D. Subramaniam, M. R. Scholz, J. Sánchez-Barriga, A. Varykhalov, S. Blügel, O. Rader, and M. Morgenstern, Probing two topological surface bands of Sb_2Te_3 by spin-polarized photoemission spectroscopy, *Physical Review B* **86**, 235106 (2012).
- [57] F. Yang, Y. R. Song, H. Li, K. F. Zhang, X. Yao, C. Liu, D. Qian, C. L. Gao, and J.-f. Jia, Identifying magnetic anisotropy of the topological surface state of $\text{Cr}_{0.05}\text{Sb}_{1.95}\text{Te}_3$ with spin-polarized STM, *Physical Review Letters* **111**, 176802 (2013).

Supplementary Information

EXPERIMENTAL METHODS

Single crystal growth

Single crystals of Sb_2Te_3 were synthesized from ultrapure ($\geq 99.999\%$) elemental Sb and Te via a self-flux technique, with nominal V doping 1% [29]. We perform measurements on three crystals from the same growth batch: sample 1 [Fig. 1(b-d), Fig. S1(a)], and sample 2 [Figs. S1(b,c), 3, and 4(a,b)], sample 3 [Fig. 2(a,b,d)].

Scanning tunneling microscopy / spectroscopy (STM/S) measurements

Single crystals are cleaved at cryogenic temperatures before inserting into STM. We perform all measurements using commercially cut PtIr tips. The local density of states (LDOS) of the sample surface is measured via STS by locally resolved dI/dV curves using standard lock-in technique. The bias modulation frequency is 1.115 kHz, and the zero-to-peak amplitudes are explicitly stated in the figure captions in the main text.

Landau level fitting

Different choices of fitting ranges and background polynomial orders lead to slight variations in the extracted peak values. Fig. 3(b,c) present a representative set of LL parameters obtained using one consistent peak-extraction procedure.

DENSITY FUNCTIONAL THEORY CALCULATIONS

We perform first-principles calculations within Density Functional Theory (DFT) using the Vienna *Ab initio* Simulation Package (VASP) [32, 33]. We adopt the Perdew–Burke–Ernzerhof (PBE) generalized-gradient approximation (GGA) [34] for the exchange-correlation functional and describe electron-ion interactions with the projector augmented-wave (PAW) method [48]. The slab model consists of 10 quintuple layers (QLs) of Sb_2Te_3 , separated by a 15 Å vacuum layer along the z direction. We use a plane-wave cutoff energy of 200 eV and sample the Brillouin zone with a Γ -centered $11 \times 11 \times 1$ Monkhorst–Pack grid.

Band-Structure Calculation

We include spin–orbit coupling (SOC) to reproduce the band inversion at the Γ point that generates the Dirac surface state in the bulk energy gap. The electronic band structure is computed along the high-symmetry path $\text{K}–\Gamma–\text{M}$, allowing us to identify the bands associated with the topological surface state. We have used VASPKIT in the postprocessing process [49].

Wave-Function–Density Analysis Near the Γ Point

To characterize the depth dependence of the topological surface state, we evaluate its wave-function density (WFD) on a dense set of k points near the Γ point. For each point k and band index b , VASP provides the projected wave-function weight $|\psi_{k,b}^{(i)}|^2$ on each atom i . For the atom i_L in atomic layer L , we define the layer-resolved, k -averaged wave-function density as

$$\text{WFD}_{\text{avg}}(L) = \frac{1}{N_k N_{\text{bands}}} \sum_{k=1}^{N_k} \sum_{b=1}^{N_{\text{bands}}} \left| \psi_{k,b}^{(i_L)} \right|^2, \quad (\text{S1})$$

where $N_{\text{bands}} = 2$ is the number of bands forming the Dirac cone. The quantity $\text{WFD}_{\text{avg}}(L)$ therefore measures the average probability density of the topological surface-state wave function on layer L .

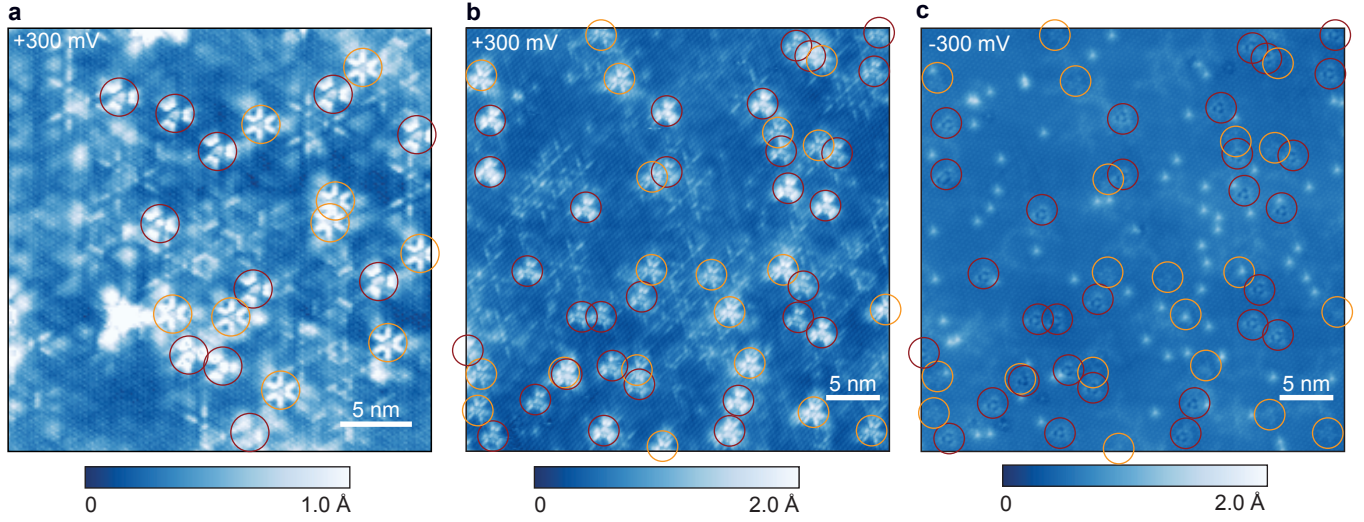


FIG. S1. V impurity concentration determination. (a) The same $30 \times 30 \text{ nm}^2$ STM topography as Fig. 1(b) in the main text. Red and orange circles mark Type I and Type II impurities, respectively. We identify 11 Type I defects (0.198%) and 9 Type II defects (0.162%). (b, c) STM topographies acquired over a $40 \times 40 \text{ nm}^2$ region. We identify 30 Type I defects (0.3%) and 20 Type II defects (0.2%). STM setpoints: $V_{\text{sample}} = +300 \text{ mV}$, $I_{\text{set}} = 100 \text{ pA}$ for (a); $V_{\text{sample}} = +300 \text{ mV}$, $I_{\text{set}} = 30 \text{ pA}$ for (b); and $V_{\text{sample}} = -300 \text{ mV}$, $I_{\text{set}} = 30 \text{ pA}$ for (c).

SUMMARY OF DEPTH PROBING OF TOPOLOGICAL SURFACE STATES

In Table I, we summarize previous studies on determining the depth of topological surface states (SS) in various materials, including (doped) topological insulators (TIs), magnetic topological insulator (MTI), topological crystalline insulators (TCIs), and topological Kondo insulator (TKI). In Table II, we summarize previous studies on Sb_2Te_3 with various synthesis and characterization methods.

Material	SS depth	Method	Reference
Sb	≈ 3 BL ^(a)	MBE + STM	Yao, Sci. Rep. (2013) [50]
Bi_2Se_3 , Bi_2Te_3	≈ 1 nm	<i>ab initio</i> calculation	Urazhdin, PRB (2004) [5]
$(\text{Bi}, \text{Sb})_2\text{Te}_3$, Bi_2Se_3	a few QLs	<i>ab initio</i> calculation	Zhang, Nat. Phys. (2009) [6]
Bi_2Se_3	≈ 3 QL	MBE + ARPES	Zhang, Nat. Phys. (2010) [15]
Bi_2Se_3	≈ 2 nm	Time-resolved ARPES + SPV	Ciocys, npj Quant. Mat. (2020) [18]
Bi_2Te_3	≈ 1 QL	MBE + ARPES	Li, Adv. Mat. (2010) [14]
Sb_2Te_3	≈ 2 QL	MBE + STM	Jiang, PRL (2012) [23]
Sb_2Te_3	< 10 nm	MBE + transport	Takagaki, PRB (2012) [10]
Sb_2Te_3	≈ 2 QL	gate-tunable MBE + STM	Zhang, PRL (2013) [24]
$\text{Bi}_{1-x}\text{Sb}_x$	≈ 4 nm	MBE + THz spectroscopy	Park, Adv. Sci. (2022) [22]
$\text{Sb}_2(\text{Te}_{1-x}\text{Se}_x)_3$	≈ 2 nm	<i>ab initio</i> calculation	Zhang, NJP (2010) [7]
$(\text{Bi}_{1-x}\text{In}_x)_2\text{Se}_3$	≈ 3 QL	MBE + THz spectroscopy	Wu, Nat. Phys. (2013) [21]
$(\text{Bi}_{1-x}\text{In}_x)_2\text{Se}_3$	≈ 3 QL	MBE + ARPES	Wang, Nano Lett. (2019) [19]
Cr- $(\text{Bi}, \text{Sb})_2\text{Te}_3/\text{FeTe}$	< 4 QL	MBE + transport etc.	Yi, Science (2024) [51]
$(\text{Bi}_{1-x}\text{Sb}_x)_2\text{Te}_3$	≥ 3 nm	MBE + transport	van Veen, PRB (2025) [13]
MnBi_2Te_4	a few SLs	DFT + Monte Carlo	Otrokov, PRL (2019) [8]
MnBi_2Te_4	≈ 2 SL	<i>ab initio</i> calculation	Sun, PRB (2020) [9]
MnBi_2Te_4	≈ 1 SL	MBE + ARPES	Xu, Nano Lett. (2022) [20]
$\text{Pb}_{1-x}\text{Sn}_x\text{Se}$	$< \text{one slab}$	ARPES	Dziawa, Nat. Mat. (2012) [16]
SnTe	a few nm	MBE + transport	Assaf, App. Phys. Lett. (2014) [11]
SnTe	< 10 nm	MBE + ARPES	Gong, Nano Res. (2018) [17]
Bi_4Br_4	2.1 nm	STM	Shumiya, Nat. Mat. (2022) [52]
SmB_6	10-15 nm	point contact spectroscopy	Lee, Nature (2019) [53]
SmB_6	32 nm	sputtering + SP + transport	Liu, PRL (2018) [12]

^(a) Penetration depth λ is k -dependent.

TABLE I. Previous studies of the topological SS depth in various candidates. QL: quintuple layer; SL: septuple layer; MBE: molecular-beam epitaxy; ARPES: angle-resolved photoemission spectroscopy; SPV: surface photovoltage effect; STM: scanning tunneling microscopy; MFM: magnetic force microscopy; DFT: density functional theory; SP: spin pumping.

Sb₂Te₃ Material	Method	E_g (meV)	v_D (m/s)	Δ (meV)	Reference
MOCVD on Al ₂ O ₃ , 750 nm	ARPES	n/a (above E _F)	2.7 × 10 ⁵	–	Bendt, JMCA (2014) [54]
MBE on Si(111), 50 QL	ARPES	n/a (above E _F)	4.1 × 10 ⁵ ^(a)	–	Wang, Nano Res. (2010) [55]
MBE on 6H-SiC(0001), 50 QL	STM <i>dI/dV</i>	~ 300	–	–	Jiang, PRL (2012) [30]
MBE on 6H-SiC(0001), 7 QL	STM LLS	~ 300	4.3 × 10 ⁵	–	Jiang, PRL (2012) [23]
cleaved single crystal	ARPES & STM <i>dI/dV</i>	200	3.8 ± 0.2 × 10 ⁵	–	Pauly, PRB (2012) [56]
cleaved single crystal	STM LLS	200	4.5 × 10 ⁵ ^(b)	–	Pauly, PRB (2015) [36]
(Cr _x Sb _{1-x}) ₂ Te ₃ , <i>x</i> = 2.5%, cleaved single crystal	STM LLS	–	–	0	Yang, PRL (2013) [57]
Cr-surface-doped Sb ₂ Te ₃ , MBE on 6H-SiC(0001), 50 QL	STM LLS	~ 300	4.8 × 10 ⁵	0–12 ^(c)	Jiang, PRB (2015) [26]
Cr _y (Bi _{0.1} Sb _{0.9}) _{2-y} Te ₃ , <i>y</i> = 0.08, cleaved single crystal	STM QPI	–	4.4 × 10 ⁵	10–44 ^(d)	Lee, PNAS (2015) [25]
(V _x Sb _{1-x}) ₂ Te ₃ , <i>x</i> = 0.75%, cleaved single crystal	STM LLS	~ 150	–	16	Sessi, Nat. Com. (2016) [27]
(V _x Sb _{1-x}) ₂ Te ₃ , <i>x</i> = 0.23%, cleaved single crystal	STM LLS	240 ± 5	4.8 ± 0.1 × 10 ⁵	–	this work

- ^(a) v_D decreases from 4.8×10^5 m/s for 3 QL films down to 4.1×10^5 m/s for bulk-like 50 QL films. All velocity measurements are below E_D , because the empty states above E_D are not accessible in ARPES.
- ^(b) Value given for full-range LL fit from $-3 \leq n \leq 6$. For $n < 0$ only, $v_{D-} = 4.9 \times 10^5$ m/s; for $n > 0$ only, $v_{D+} = 4.1 \times 10^5$ m/s.
- ^(c) For Cr substitution at top-layer Sb sites only, with Δ increasing approximately linearly for $x = 0, 3\%, 6\%, 9\%, 12\%, 15\%, 18\%, 21\%$.
- ^(d) Local Δ increases approximately linearly as local y increases from 0.02 to 0.21. This corresponds to $x = 1\%$ to 10% Cr substitution at Bi/Sb sites.

TABLE II. Measurements of bulk gap E_g , surface state velocity v_D , and surface state mass gap Δ in Sb₂Te₃.